

Chapter 5

Ring-jet structure and wavelet analysis

5.1 Introduction

One of the primary objectives of this investigation is to understand the cluster structures, if any, present in our experimental data. It has been speculated that the emission of Cerenkov gluons within the intermediate fireball might be a primary source of local density fluctuations and therefore might be a source of cluster formation [1]. An alternative but somewhat similar speculation is the formation of a shock wave traveling through the partonic/nuclear medium of the fireball [1, 2]. These macroscopic phenomena correspond respectively, to the transverse and longitudinal excitations of the medium concerned. In either case however, the emission pattern is characterized by a conical structure defined in terms of a semi-vertex angle ξ as,

$$\cos \xi = \frac{c_{med}}{v} = \frac{c}{\mu v} \quad (5.1)$$

Here depending upon the case, as it may be, c_{med} is either the velocity of the gluon or that of the shock wave in the fireball medium, v is the velocity of the partonic/hadronic jet that triggers either the Cerenkov gluon or the shock wave emission, μ is the refractive index of the medium concerned, and c is either the velocity of the gluon in vacuum or the velocity of sound wave in air. The incident nucleus can be treated as a bunch of quarks, each of which is capable of emitting Cerenkov gluons while traversing through the target nucleus.

Experimentally the real part of the elastic forward scattering amplitude of all hadronic processes in high-energy collisions have been found to be positive [3]. This condition is necessary for the Cerenkov emission to take place, as the excess of nuclear refractive index over unity is proportional to the real part of the forward scattering amplitude. Under favorable circumstances the conical structure, if so formed, may withstand the impact of collision and retain its original shape. If the initial/triggering parton direction is same as that of the incident beam, and if the number of minijet emitting gluons is large, then in the distributions of the particles one may observe ring-like structures that are clustered within narrow regions of pseudorapidity (η). The particles may however be distributed more or less uniformly over the entire azimuth $\varphi \in [0, 2\pi]$. On the other hand, if the number of jet emitting gluons is small, then it is more likely that several jets, each restricted to narrow intervals of both η and φ , will be formed, resulting thereby jet-like structures in the distributions of final state hadrons. A quark-gluon jet created by a high-energy parton can as well give rise to a collective behavior that is similar to the Mach shock wave formation. For thin targets like the nuclei, due to their small confinement lengths, just like the Cerenkov gluons shock wave emission can also take place [4]. A partonic jet moving with a velocity close to that of the light can be considered as a body moving in the nuclear/partonic medium with a supersonic speed, which may cause a large pressure variation, and therefore can give rise to shock waves. The Mach angle depends upon the state of the matter through which the partonic jets are moving. Once again depending on the nature of the medium, the sound (elastic) wave speed is expected to vary in between $0.4c - 0.9c$ [5].

The wavelet analysis technique is mainly used in signal processing, image analysis, communication systems, fractals and in several other branches of physics. For a review one can for example see [6, 7]. The wavelets have also been used for pattern recognition in high-multiplicity AB events [8, 9]. The key idea of wavelet analysis is the expansion of the signal with respect to a self-similar set of orthogonal basis functions, the so-called wavelets. The entire basis is constructed through dilation and translation of one single function, known as the mother wavelet. It provides a convenient representation to study self-similar processes, in which an arbitrary distribution can be resolved simultaneously in many scales. Singularities, i.e. large fluctuations can be identified through wavelet decomposition, as and where the wavelet coefficients are large. At lower (higher) resolution wavelet algorithm returns gross (finer) pictures of the signal under scrutiny. In this chapter, along with an analysis on the angular distributions of the shower tracks in the context of ring and/or jet like structures, we also present some results obtained from a wavelet analysis in the context of cluster formation. In order to study any unusual structure in the particle emission data, we compare the results obtained from ^{16}O -Ag/Br and ^{32}S -Ag/Br interactions at an incident energy $E_{lab} = 200$ GeV/nucleon. We also compare the experiments with the UrQMD and UrQMD+BEC simulations.

5.2 Literature review

Ring-like structures were first studied in a cosmic-ray induced nuclear interaction [10]. Subsequently in several accelerator based experiments ring and jet-like structures were further investigated in high-energy AB interactions [11–16]. The results of azimuthal structure analysis in $^{16}\text{O-Ag/Br}$, $^{32}\text{S-Ag/Br}$ and $^{32}\text{S+Au}$ interactions at $200A$ GeV/c (EMU01 experiment) were compared with the FRITIOF-1.7 simulations taking the γ -conversion and HBT effects into account [11]. It was observed that the FRITIOF model combined with the γ -conversion factor, could reproduce the experimental data well, while the effect of HBT was found to be marginal. In $^{197}\text{Au+Ag/Br}$ interactions at $11.6A$ GeV/c ring-like structures were observed in the target azimuth [17]. The angular structure of particle emission in $^{208}\text{Pb+Ag/Br}$ interaction at $158A$ GeV/c obtained from EMU12 experiment [18] was investigated by Vokál, *et al.* [19], and the data were compared with the FRITIOF model. These results also supported the presence of ring-like substructures in the target azimuth, and the creation mechanism of such substructures are similar to that of the Cerenkov radiation. The EMU12 data also suggest that there are two preferred regions of pseudorapidity where ring-like events are observed, one in the forward and another in the backward hemisphere in the center-of-mass system. The ring/jet-like structures were also studied in $^{28}\text{Si-Ag/Br}$ interaction at $14.5A$ GeV and in $^{32}\text{S-Ag/Br}$ interaction at $200A$ GeV [20]. The experimental results were compared with the RQMD and UrQMD models where the BEC effect was also taken into account. There was an indication of ring-like structures being present in the $^{28}\text{Si-Ag/Br}$ interaction, while in the $^{32}\text{S-Ag/Br}$ interaction jet-like structures were found. The microscopic transport models could not match the experiments.

In high multiplicity AB events cluster structures in multiparticle emission data were studied with the help of wavelet analysis [8, 21–23]. The pseudorapidity distributions in the JACEE events were analyzed in terms of the wavelet transform technique [24]. The wavelet spectra of one Ca-C and another Si-Ag/Br event were compared with Monte-Carlo simulations using Poisson distributed random numbers, uniformly distributed random numbers and a p -model. The experimental results followed a trend similar to that observed in the uniformly distributed random numbers as well as in the Poisson distributed random numbers [21]. The wavelet results obtained from the EMU15 Pb+Pb data at 158 GeV/nucleon showed the presence of ring and jet-like structures in some of the high multiplicity events [25]. A two-dimensional wavelet analysis of a high-multiplicity Pb+Pb event at 158 GeV/nucleon (EMU15 experiment) [26] has been presented in [27]. In [27] the (η, φ) -space was divided into 24 equal sectors. In each sector the wavelet power spectra was calculated and the most densely populated regions in the (η, φ) -plane was identified. The g_2 wavelets (second derivatives of the Gaussian function) were used to analyze the Au+Emulsion data at $11.6A$ GeV/c

[28]. Some irregularities in the wavelet pseudorapidity spectra were observed, which were attributed to the preferred emission angles of groups of particles [28]. The wavelet technique was used to analyze the data acquired from the EMU12 experiment [18]. The observations of EMU12 experiment were more or less similar to that of [28]. The pseudorapidity distributions of shower tracks in $^{28}\text{Si-Ag/Br}$ and $^{32}\text{S-Ag/Br}$ interactions, respectively at 14.5A GeV and 200A GeV, were analyzed by using the continuous wavelet transform technique [29]. In this investigation experimental results were compared with UrQMD where the BEC effect was mimicked into the simulation. Presence of some non-trivial effects was found in the particle emission data that was beyond the UrQMD or UrQMD+BEC prediction. There are some reports where wavelet technique has also been employed to study particle correlations [8, 9, 30].

5.3 Ring and jet-like structures

The method of ring-jet analysis has been elaborated in [11]. A brief description of the same is presented below only for the sake of completeness. For an individual event, we start with a fixed number ($n \leq n_s$) of particles (shower tracks). Each n -tuple of particles is sequentially arranged either in the ascending or descending order along the η -axis. This subgroup of particles is then characterized by a size $\Delta\eta = |\eta_{m+i-1} - \eta_i|$, $i = 1 \cdots n_s$, a mean $\eta_m = \sum_{i=1}^n \eta_i/n$, and a density $\rho = n/\Delta\eta$. Each subgroup of particles having same multiplicity n can be statistically compared with each other. The azimuthal structure of a particular subgroup can be parameterized in terms of the following quantities,

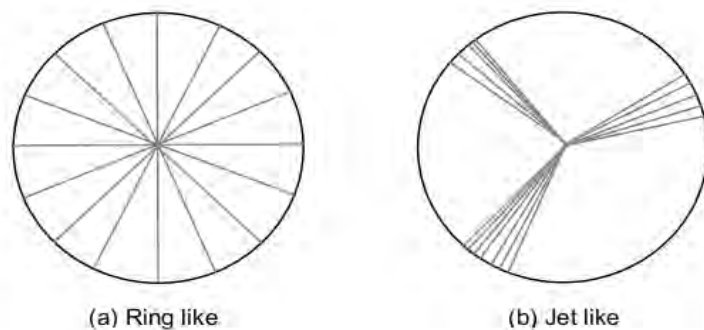


Figure 5.1: Schematic representation of (a) a ring-like distribution and (b) a jet-like distribution of tracks in the target azimuth.

$$S_1 = - \sum_{i=1}^n \ln(\Delta\varphi_i) \quad \text{and} \quad S_2 = \sum_{i=1}^n (\Delta\varphi_i)^2 \quad (5.2)$$

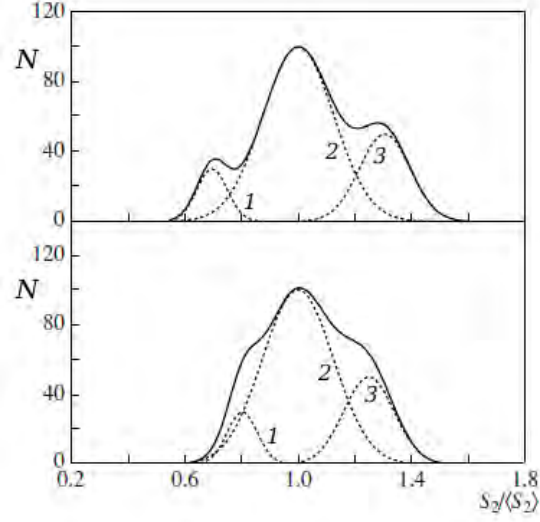


Figure 5.2: A schematic of $S_2/\langle S_2 \rangle$ distributions obtained for three cases, namely (1) ring-like events, (2) stochastic distribution and (3) jet-like events. The solid curve represents the resultant distribution.

Here $\Delta\varphi_i$ is the φ -difference of two neighboring particles, i.e., between the i -th and the $(i+1)$ -th particle belonging to a particular subgroup, starting from first and second and ending at the n -th and first. One can measure φ in units of a complete revolution [$\varphi \in (0, 2\pi)$]. Each $\Delta\varphi_i$ would then be a fraction of the total azimuth 2π . The difference between a ring-like and a jet-like structure has been schematically explained in Figure 5.1 using the target azimuth. For a ring-like structure the tracks are almost isotropically distributed over the entire azimuth. On the other hand for a jet-like structure some of the tracks are clustered within a narrow region of φ , but each cluster is well separated from the other in the azimuthal plane. Note that for a perfect ring-like emission of particles both $S_1 \rightarrow n \ln n$ and $S_2 \rightarrow 1/n$ will be small valued. On the other hand for a perfect jet-like emission $S_1 \rightarrow \infty$ and $S_2 \rightarrow 1$. While S_1 is sensitive to small gaps S_2 is sensitive only to large gaps. For a purely stochastic emission the $\Delta\varphi$ -distribution is given by [11, 31],

$$f(\Delta\varphi)d(\Delta\varphi) = (n-1)(1-\Delta\varphi)^{(n-2)}d(\Delta\varphi) \quad (5.3)$$

The expectation values of the S -parameters are therefore given by,

$$\langle S_1 \rangle = n \sum_{k=1}^{n-1} \frac{1}{k} \quad \text{and} \quad \langle S_2 \rangle = \frac{2}{n+1} \quad (5.4)$$

The distributions of S_1 and S_2 would be peaked around the corresponding expectation values. Presence of jet-like substructures would result in bulging and small local peaks in the distributions to the right side, whereas ring-like substructures would do the same

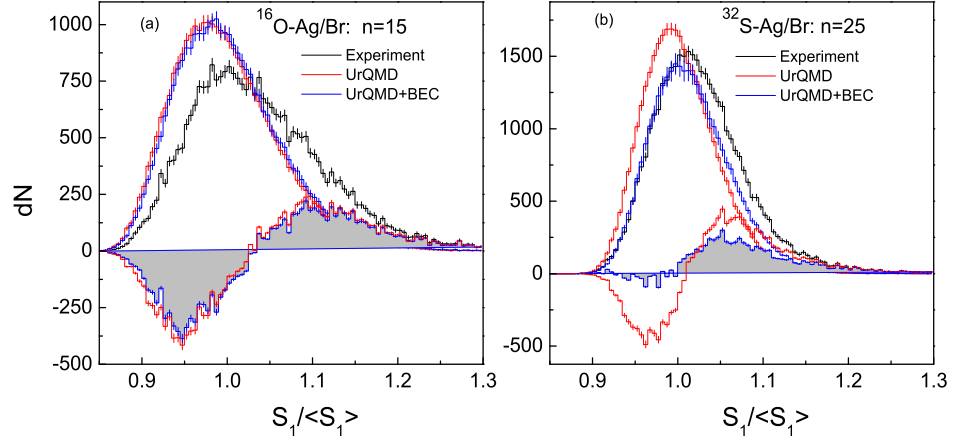


Figure 5.3: Distributions of the S_1 parameter normalized by its stochastic expectation value $\langle S_1 \rangle$ for (a) $^{16}\text{O-Ag/Br}$ and (b) $^{32}\text{S-Ag/Br}$ interactions both at 200A GeV/c. The shaded region is experimental excess over UrQMD+BEC distribution and without shaded region is over UrQMD.

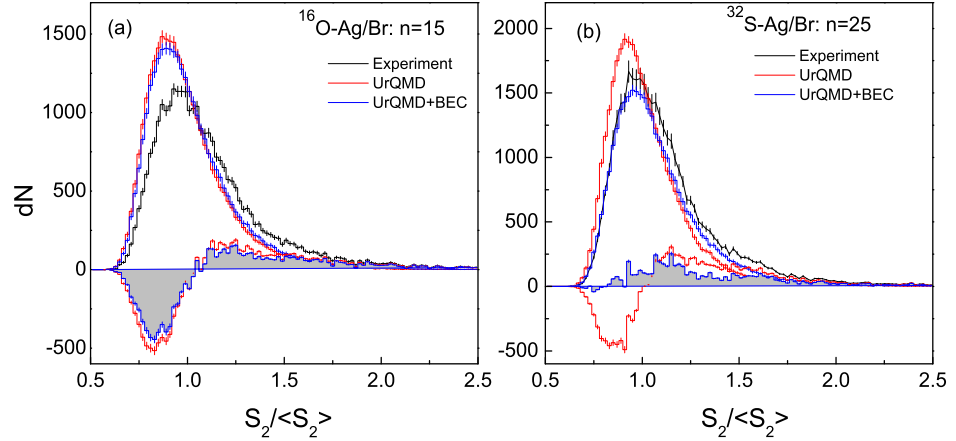


Figure 5.4: Same as in Figure 5.3 but for the S_2 parameter.

towards the left side of the expectation values. A schematic of the distributions of S_2 expected from three different processes are shown in the Gaussian form in Figure 5.2. In this figure the distributions marked by 1, 2 and 3 (dotted lines) represent, respectively the ring-like, stochastic and jet-like structures. All three distributions are then combined to form a resultant distribution. In order to extract the information about any unusual azimuthal structure, one therefore needs to first eliminate the contributions coming from the stochastic processes.

We have taken $n = 15$ and 25, respectively for the $^{16}\text{O-Ag/Br}$ and $^{32}\text{S-Ag/Br}$ event samples. For these choices of n the stochastic expectation values [see Equation (5.4)] come out as $\langle S_1 \rangle \approx 48.8$ and 94.4, and $\langle S_2 \rangle \approx 0.125$ and 0.077 respectively. Distributions of the S_1 parameter normalized by the corresponding stochastic expectation value $\langle S_1 \rangle$ are plotted in Figure 5.3 for both interactions. For a particular interaction the experiment, the UrQMD

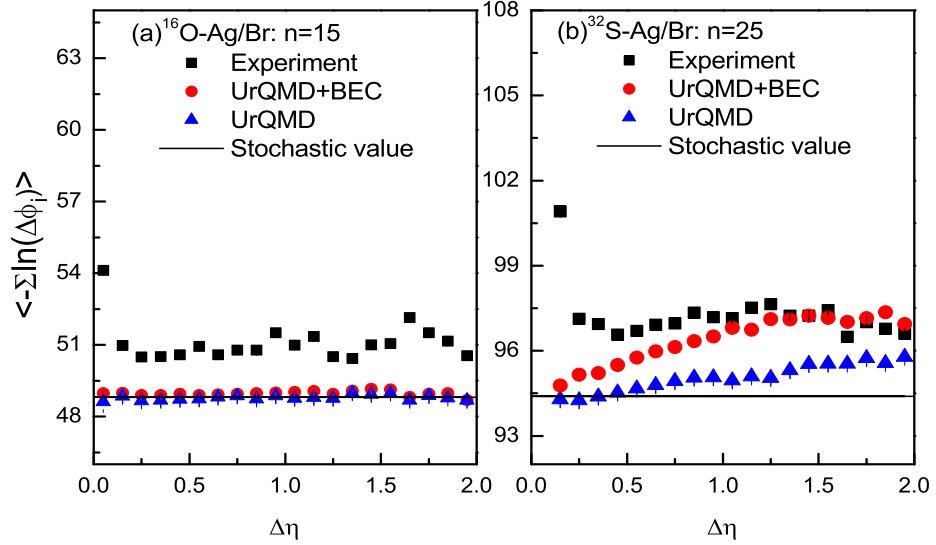


Figure 5.5: Average behavior of the S_1 parameter $\langle -\sum \ln(\Delta\phi_i) \rangle$ for (a) $^{16}\text{O-Ag/Br}$ and (b) $^{32}\text{S-Ag/Br}$ interactions both at 200A GeV/c.

and UrQMD+BEC generated distributions are plotted together. As expected the UrQMD and UrQMD+BEC generated distributions peak around $S_1/\langle S_1 \rangle = 1.0$. The simulated distributions are taller, smoother and slightly narrower than the $^{16}\text{O-Ag/Br}$ experiment. On the other hand in the $^{32}\text{S-Ag/Br}$ case the UrQMD generated distribution is slightly taller while the UrQMD+BEC generated distribution is slightly shorter than the corresponding experimental distribution. All distributions are asymmetric, slightly right skewed, and the asymmetry is more pronounced in the experimental distributions. In each case the experimental distribution is slightly shifted towards right with respect to the corresponding simulation(s). Large S_1 values in the experimental distributions signify presence of jet-like structures. The differences between the experiment and the respective simulated data are also shown in these figures. We find experimental excesses in the $S_1/\langle S_1 \rangle > 1.0$ region, a feature common to both the interactions. In the $S_1/\langle S_1 \rangle < 1.0$ region of the $^{16}\text{O-Ag/Br}$ interaction both UrQMD and UrQMD+BEC simulations overpredict the experiment. On the other hand in the $^{32}\text{S-Ag/Br}$ case, only the UrQMD simulation has an excess whereas the UrQMD+BEC simulation matches reasonably well with the experiment. In Figure 5.4 graphical plots of $S_2/\langle S_2 \rangle$ are shown. The behavior is more or less same as that of the $S_1/\langle S_1 \rangle$ distributions. In both interactions there are slight experimental excesses over the corresponding simulated distributions in the right side of the peak ($S_2/\langle S_2 \rangle > 1.0$). In the left side of the peak ($S_2/\langle S_2 \rangle < 1.0$) both the simulations exceed the experiment in the $^{16}\text{O-Ag/Br}$ case, whereas in the $^{32}\text{S-Ag/Br}$ case only the UrQMD over-predicts the experiment, whereas the experiment marginally exceeds the UrQMD+BEC distribution. The overall nature of the distributions of S -parameters indicates the presence of jet-like structures in the target azimuth, the contribution however is small.

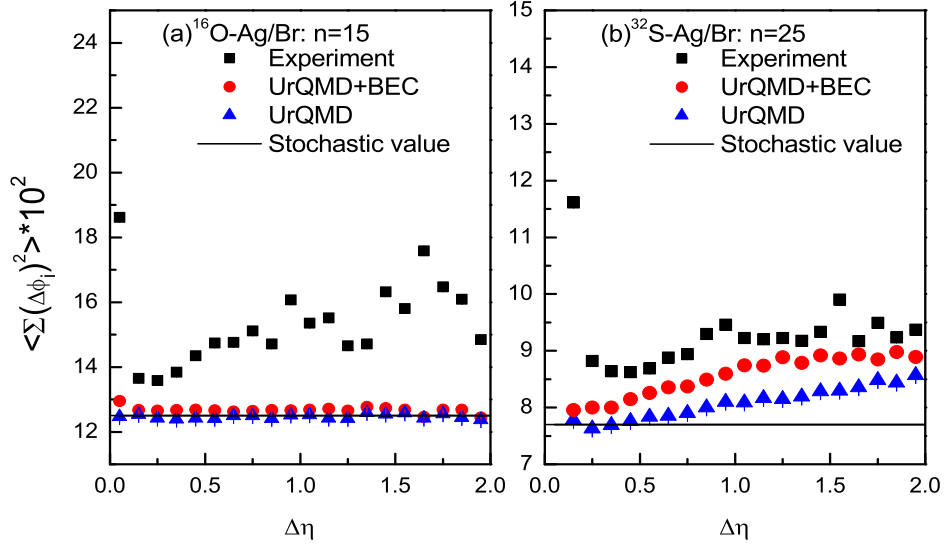


Figure 5.6: Same as in Figure 5.5 but for the S_2 parameter.

The variations of $\langle -\sum \ln(\Delta\varphi_i) \rangle$ and $\langle \sum (\Delta\varphi_i)^2 \rangle$ against $\Delta\eta$ are shown respectively, in Figure 5.5 and Figure 5.6 for both the interactions. Note that these quantities are different from the stochastic expectations values, $\langle S_1 \rangle$ and $\langle S_2 \rangle$. The dashed lines in these figures correspond to Equation (5.4). The UrQMD and UrQMD+BEC results are also included in these diagrams. One can see that the experimental values lie consistently above the stochastic expectation values. For the $^{16}\text{O-Ag/Br}$ interaction the simulated values of both parameters lie more or less around the corresponding stochastic expectation lines. On the other hand in the $^{32}\text{S-Ag/Br}$ case they are slowly increasing with $\Delta\eta$. At large $\Delta\eta$ the UrQMD+BEC values even lie in the range of the experiment. However, inadequacy of an independent emission model of the particles to replicate the experimental results is clearly visible in our analysis. It has been observed that to a large extent the experimentally observed average behavior of the S -parameters can be reproduced by the FRITIOF model calculation, where γ -conversion and the Hanbury-Brown-Twiss (HBT) effect have been included [11]. However, it has also been argued that before coming to a definite conclusion regarding such azimuthal structures, along with the average behavior of the S -parameters detailed distributions of some other relevant cluster parameters should be examined [15, 16].

The cluster size of the azimuthal substructures can be investigated with the help of their distributions against $\Delta\eta$. For both the interactions under our consideration, these distributions are plotted in Figures 5.7 and 5.8. A distinction between the ring and jet-like structures has been made by separating the $S_2/\langle S_2 \rangle < 1$ and $S_2/\langle S_2 \rangle > 1$ categories. These distributions are once again right skewed, having a rapid growth in the left to the peak followed by a comparatively slower fall on the right side. The width of the experimental distribution in each case is more or less same as that of the UrQMD and UrQMD+BEC distributions. For

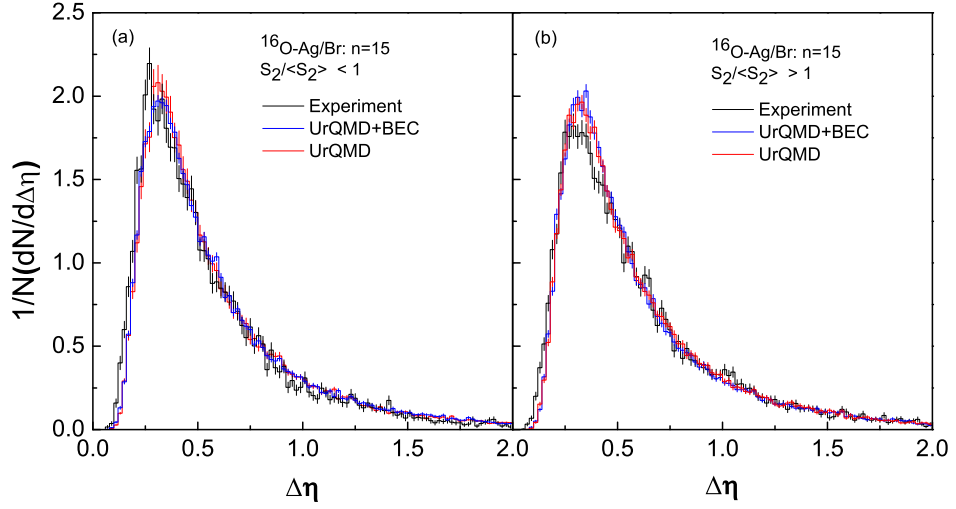


Figure 5.7: Cluster density distributions for (a) the ring-like region, $S_2/\langle S_2 \rangle < 1$ and (b) the jet-like region, $S_2/\langle S_2 \rangle > 1$ for ^{16}O -Ag/Br interactions at $200A$ GeV/c.

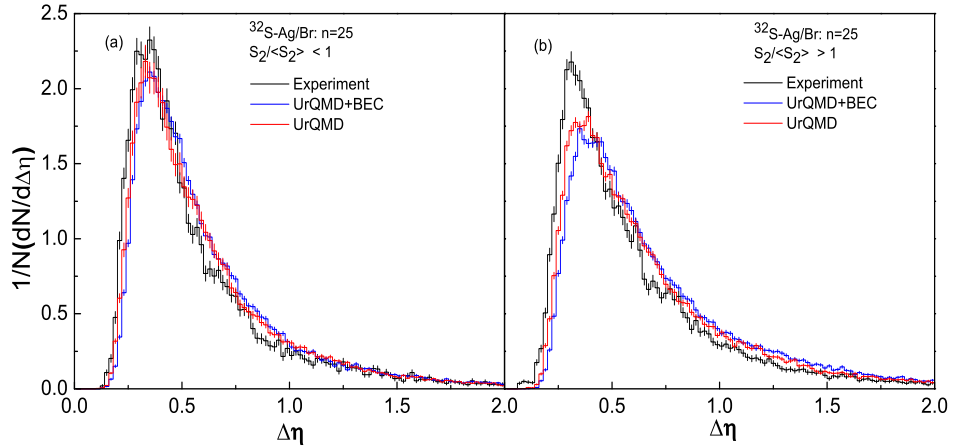


Figure 5.8: Same as in Figure 5.7 but for ^{32}S -Ag/Br interactions at $200A$ GeV/c.

both data sets one can see that small sized clusters around the peak region and to left of the peak region, have slight experimental excesses over the corresponding simulated data for the $S_2/\langle S_2 \rangle < 1$ category. On the other hand, clusters of large size (right to the peak) are either reproducible by the simulations or the simulations exceed the experimental values.

The location of jet and ring-like substructures can be investigated by studying the η_m -distributions of the S -parameters. Following the prescriptions of [15, 16] the distributions are divided into three categories, namely (i) $S_2/\langle S_2 \rangle < 0.95$, (ii) $0.95 \leq S_2/\langle S_2 \rangle \leq 1.1$ and (iii) $S_2/\langle S_2 \rangle > 1.1$. The ring-like, stochastic and jet-like structures, respectively dominate these three regions. Figure 5.9 and Figure 5.10 show the distributions of η_m for all three categories mentioned above. The average behavior of each distribution is roughly symmetric about a central value, which for each type of interaction is close to the corresponding central value of the basic η -distribution of the shower tracks. However, there are some small

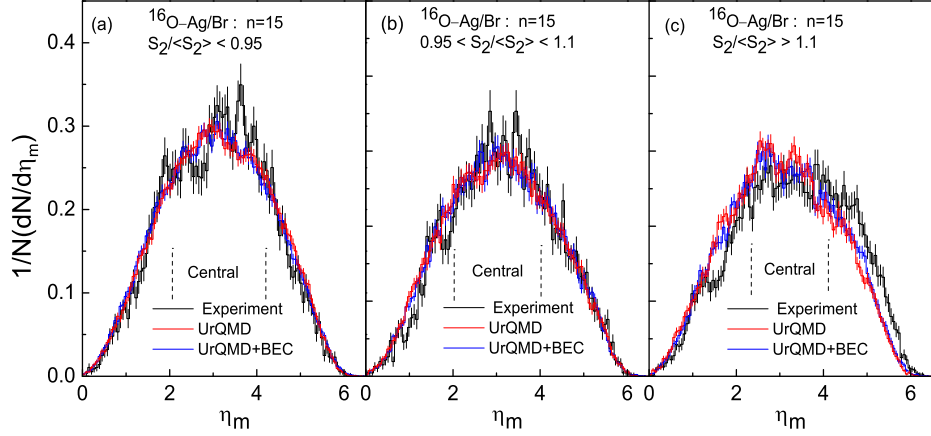


Figure 5.9: Comparison of the φ -subgroup position distributed along the η axis for three different regions of $S_2/\langle S_2 \rangle$ for ^{16}O -Ag/Br interaction at 200A GeV/c.

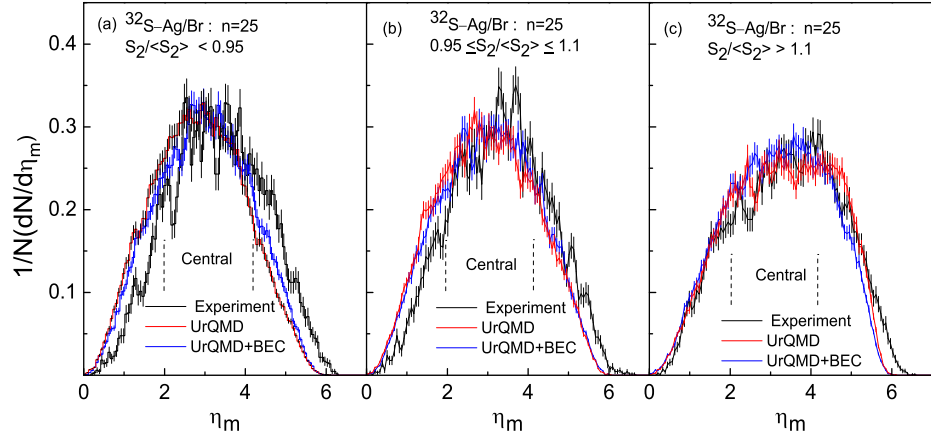


Figure 5.10: Same as in Figure 5.9 but for ^{32}S -Ag/Br interactions at 200A GeV/c.

experimental excesses beyond statistical uncertainties over the UrQMD and UrQMD+BEC simulations. For the $S_2/\langle S_2 \rangle < 0.95$ category of the ^{16}O -Ag/Br interaction, excess experimental counts are present in the form of several sharp and narrow spikes particularly around the central maximum and in the left to the central maximum regions. On the other hand for the ^{32}S -Ag/Br interaction, simulations show excess over experiment in the left to the central region, whereas in the right to the central region experiment shows excess over the simulations. The experimental excesses over the simulation can probably be attributed to ring-like substructure(s) of particle emission. However, the effect is not statistically very significant. Probably, by using a larger statistics and by choosing events for a particular centrality class, one could have reduced the noise that are otherwise present in the data. For the $0.95 \leq S_2/\langle S_2 \rangle \leq 1.1$ category, a few prominent narrow spikes are seen in the central region of the experimental distributions in both types of interactions, which cannot be replicated either by the UrQMD or by the UrQMD+BEC simulations. These structures are

more prominent in the ^{32}S induced interaction, the physical origin of which is not very much clear. For the $S_2/\langle S_2 \rangle > 1.1$ category, the experimental excesses are continuous and extend over a region of about 1 unit of η on the right-hand side of the central maxima of both interactions. This effect can be attributed to jet-like structures in the forward hemisphere.

5.4 Wavelet analysis

Wavelets are mathematical functions that can decompose signals into different frequency components so that one can study each component with a resolution matched to its scale. The mother wavelet is chosen according to the properties and patterns of the signal under consideration [6, 7]. If $\psi(x)$ is the mother wavelet then the continuous wavelet transform of a function $f(x)$ is given by,

$$W_\psi(a, b)f = \frac{1}{\sqrt{C_\psi}} \int_{-\infty}^{+\infty} f(x) a^{-1/2} \psi\left(\frac{x-b}{a}\right) dx \quad (5.5)$$

where the normalization constant

$$C_\psi = 2\pi \int_{-\infty}^{+\infty} |\tilde{\psi}(\omega)|^2 |\omega|^{-1} d\omega \quad (5.6)$$

and $\tilde{\psi}(\omega)$ is the wavelet transform of $\psi(x)$. Note that the wavelet $\psi(x)$ is characterized by a translation parameter b and a dilation parameter a . The coefficients $W_\psi(a, b)$ of the signal $f(x)$ can be interpreted as contributions of the wavelet $\psi\{(x-b)/a\}$ to the signal. Alternatively, $W_\psi(a, b)$ is a measure of the correlation between the function $f(x)$ and the mother wavelet $\psi(x)$ at the scale a and at location b . Higher correlation results in a larger coefficient and conversely. In our analysis the signal is the η -distribution of shower tracks. If we arrange the η -values of N number of tracks present in an event as $\eta_1, \eta_2, \dots, \eta_N$ etc., then the distribution of η can be expressed as,

$$f(\eta) = \frac{dn}{d\eta} = \frac{1}{N} \sum_{k=1}^N \delta(\eta - \eta_k) \quad (5.7)$$

For multiparticle data analysis derivatives of the Gaussian function like,

$$\Psi(x) \equiv g_n(x) = (-1)^{n+1} \frac{d^n}{dx^n} e^{-x^2/2} \quad (5.8)$$

are often used as mother wavelets. In particular the second derivative

$$g_2(x) = (1 - x^2)e^{-x^2/2} \quad (5.9)$$

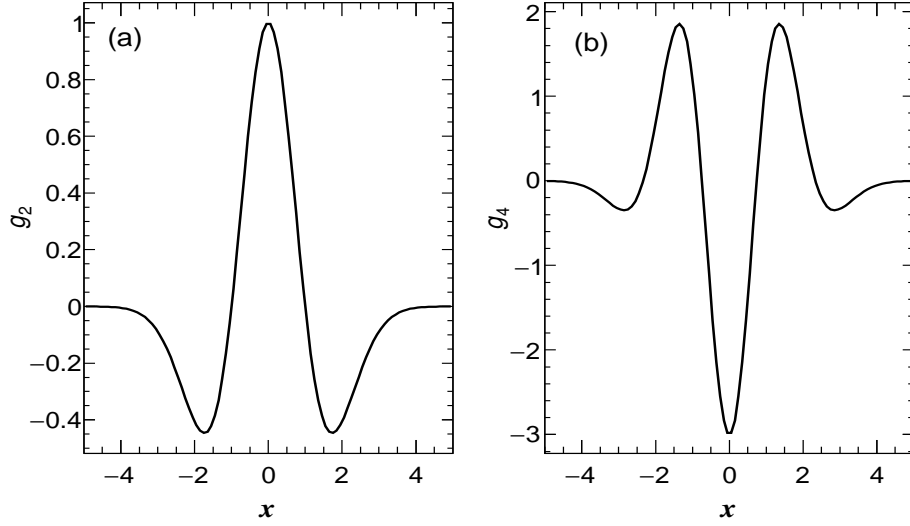


Figure 5.11: (a) Second derivative (Mexican hat wavelet) and (b) fourth derivative of the Gaussian function.

popularly known as the Mexican hat (MHAT) wavelet, and the fourth derivative

$$g_4(x) = -(x^4 - 6x^2 + 3)e^{-x^2/2} \quad (5.10)$$

are customarily used to analyze multiparticle emission data. In our analysis g_2 and g_4 are considered as the mother wavelets, the schematics of which are shown in Figure 5.11. The g_p ($p = 2$ and 4) wavelet transform of $f(\eta)$ is then given by [9],

$$W_{g_p}(a, b)f(\eta) = \frac{1}{N} \sum_{k=1}^N a^{-1/2} g_p \left(\frac{\eta_k - b}{a} \right) \quad (5.11)$$

The wavelet distributions of pseudorapidity spectra W_{g_2} are plotted in Figure 5.12 against the translation parameter b taken along the horizontal axis and the dilation parameter a taken along the vertical axis. The b -values are nothing but the locations of the particle clusters on the pseudorapidity axis. The values of wavelet coefficients are high where the gray-leveled scale has a lighter shade, and they are low where the distribution has a deeper shade. Large values of wavelet coefficient signify large number of particles crowding around a particular η -value. It is observed that the information about individual events are revealed in the small scales ($a < 0.1$), whereas in the large scales ($a > 0.5$) individual information is lost, indicating that more than one cluster combine to form a large group. For the same a -parameter, the wavelet distributions are of different intensities at different b -values, which indicates that the clustering of particles is not uniform at different locations. It is to be noted that three large groups of particles are centered around $\eta = 1.8, 2.6$ and 4.0 in the ^{16}O -Ag/Br events, and around $\eta = 2.2, 3.8$ and 5.2 in the ^{32}S -Ag/Br events. To further

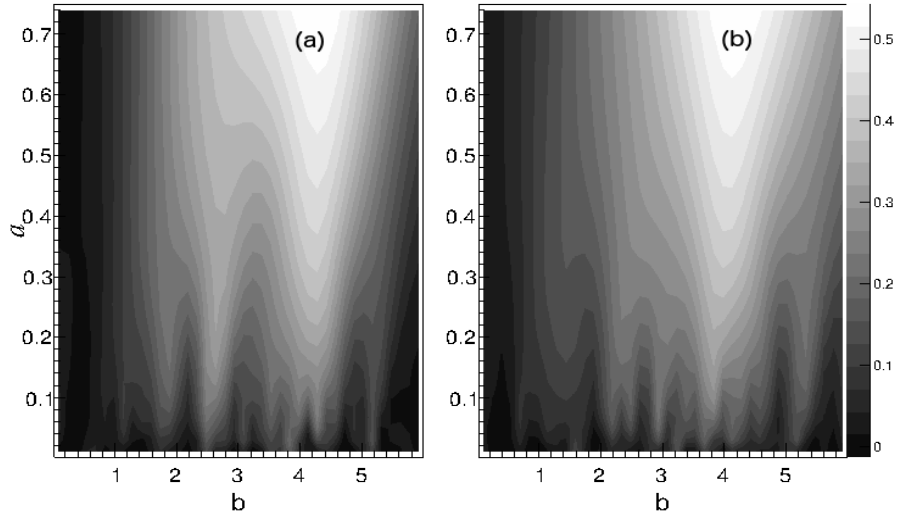


Figure 5.12: Wavelet coefficients $W_{g_2}(a, b)$ for a ^{16}O -Ag/Br event ($n_s = 202$) and a ^{32}S -Ag/Br event ($n_s = 276$) are plotted as functions of scale parameter a and translation parameter b [Equation (5.11)].

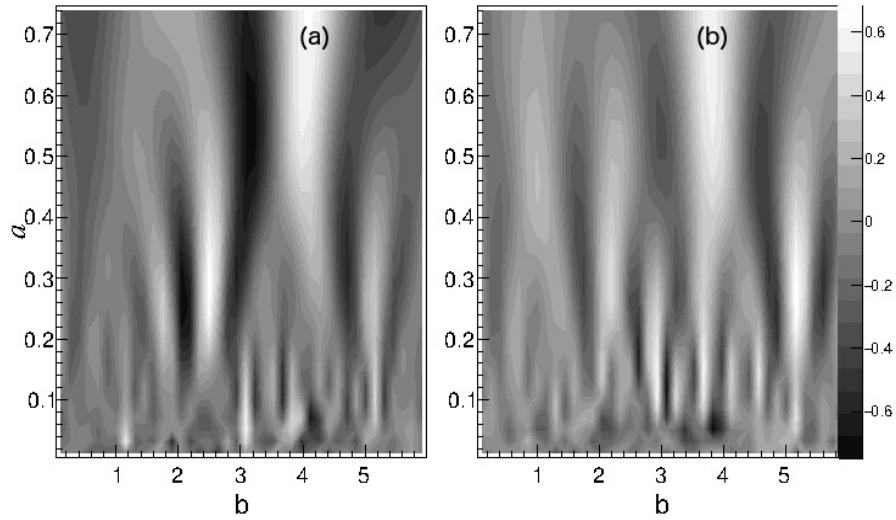


Figure 5.13: The same as in Figure 5.12 but for the g_4 wavelet.

scrutinize the cluster formation in our data, the g_4 wavelet spectra for the same events are plotted in Figure 5.13. One can see that for the ^{16}O -Ag/Br events the g_4 coefficients have several prominent maxima at $\eta = 1.2, 1.8, 2.6, 3.0, 4.0$ and 5.2 . For the ^{16}O -Ag/Br events, the local maxima of g_4 coefficients are connected with the positions of the centers of the group of particles at $\eta = 1.8$ and 2.6 in the scale range $a > 0.56$, and particles falling within $\eta = 3.0 - 4.6$ range are connected via their g_4 coefficient in the scale range $a > 0.4$. In the ^{32}S -Ag/Br events the clusterization of particles is observed at $\eta = 1.2, 2.0, 2.4, 3.0, 3.2, 3.6, 4.2, 4.6$ and 5.2 . Groups of particles having centers at $\eta = 2.0$ and 2.4 , at $\eta = 3.6, 4.2$

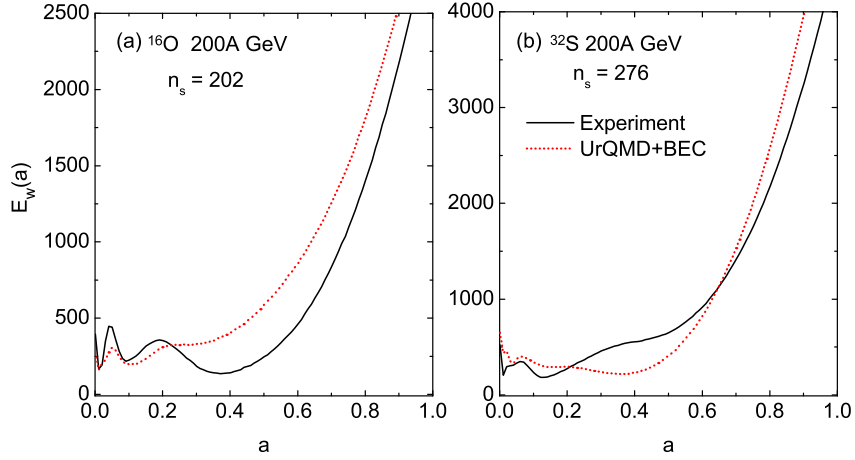


Figure 5.14: Scalograms of the events for which the g_2 wavelets are shown in Figure 5.12.

and 4.6 and the particles in the $\eta = 5.0 - 5.2$ range are connected by their wavelet maxima in the scale range $a > 0.36$. The minima at different pseudorapidity values correspond to disintegration of larger groups. Therefore, using the g_2 and g_4 spectra we can examine the cluster properties of particles at different pseudorapidity locations and at appropriate pseudorapidity resolutions. The most dominant scale at which the clusters are formed, can be obtained from the scalogram, defined as,

$$E_w(a) = \int W_{g_2}(a, b)^2 db \quad (5.12)$$

Some of the characteristic features of an event are also reflected in a scalogram. As for example, a local minimum on a scalogram represents the average distance between the particle clusters, while a local maximum signifies the most compact group of particles. Figure 5.14 shows the scalograms for the same ^{16}O -Ag/Br and ^{32}S -Ag/Br events for which the contour plots of W_{g_2} and W_{g_4} coefficients are shown respectively in Figures 5.12 and 5.13. For each event the experimental result is compared with the corresponding UrQMD+BEC simulation. In the ^{16}O -Ag/Br event the maxima occur at $a \approx 0.04$ and 0.2 , whereas the minima occur at $a \approx 0.01$ and 0.1 . In the ^{32}S -Ag/Br event the maxima occur at $a \approx 0.06$ and 0.37 , while the minima occur at $a \approx 0.01$ and 0.12 . For both the events UrQMD+BEC simulation cannot match the experiment satisfactorily. We have checked that most of the local maxima (minima) in the event samples are found within $0.05 \leq a \leq 0.5$ range, and in most of the events only a few such maxima (minima) are found.

In a wavelet analysis the g_2 spectrum plays an important role, as it can detect the coarse structures of the signal, event-wise pseudorapidity distributions in the present case. In Figure 5.15 the g_2 spectra, obtained respectively for the ^{16}O -Ag/Br and ^{32}S -Ag/Br interactions at $200A$ GeV/c are schematically presented. For each event sample the spectra are plotted

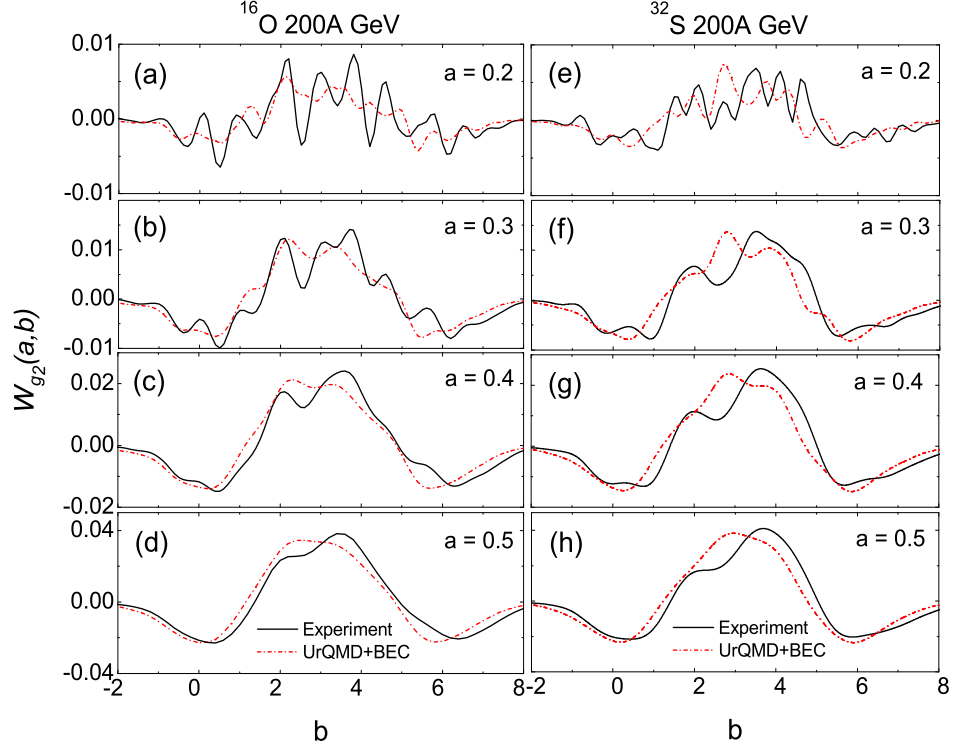


Figure 5.15: g_2 wavelet pseudorapidity spectra for ^{16}O (left) and ^{32}S (right) interactions for different values of scale parameter a . In both the cases the experimental results are compared with the corresponding UrQMD+BEC simulation.

at four different scales, $a = 0.2, 0.3, 0.4$ and 0.5 . For an easy comparison experimental results are plotted along with the corresponding UrQMD+BEC simulations. At small scale each spectrum fluctuates rapidly while with increasing scale size it gradually becomes more regular. Each distribution ultimately converges to the mother wavelet g_2 . Several peaks are seen within the $1 \leq b \leq 5$ range for both ^{16}O -Ag/Br and ^{32}S -Ag/Br experiments. Overall fluctuations in the simulated event samples are less rapid compared to the respective experiment, a fact that can clearly be noticed in Figure 5.15 at $a = 0.2$. The observed maxima of the spectra are associated with preferred pseudorapidity locations where cluster formation takes place. Clusters are present in the target fragmentation, central particle producing, and projectile fragmentation regions. The number of particles involved in separate groups can be estimated from the size of the area lying under the local maxima. To study the cluster formation further, we have graphically presented the g_4 -spectra for the ^{16}O -Ag/Br and ^{32}S -Ag/Br interactions in Figure 5.16. In each diagram the experimental and simulated results are compared. We see more rapid fluctuations than the g_2 spectra at a particular resolution. The locations of maxima (minima) are more or less in the same range of b as they are in the g_2 -spectra. In the g_4 -spectra there are however more number of peaks than that in the corresponding g_2 -spectra. The other features of the g_4 wavelet spectra are more or less same as that of the g_2 -wavelet. Peaks in the target fragmentation, the central

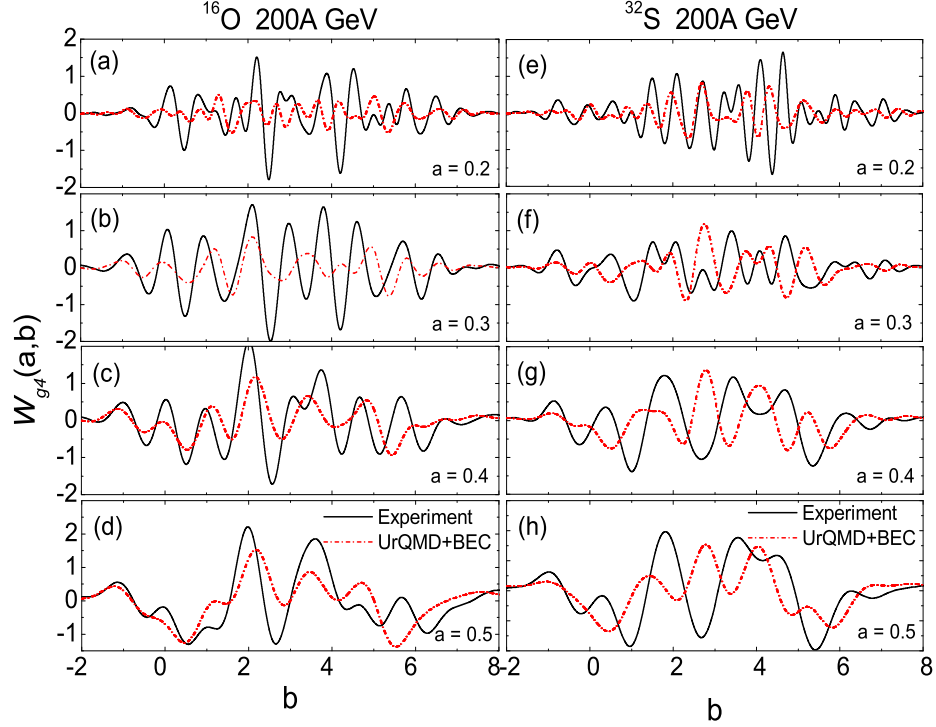


Figure 5.16: The same as in Figure 5.15 but for the g_4 wavelet.

particle producing, and projectile fragmentation regions are clearly observed in the wavelet g_4 -spectra too for both interactions. In this case also the simulated results cannot exactly replicate the experimental results.

The results described above enable us to fix the characteristic scales and the preferred pseudorapidity locations where particle clusters are formed. Using the scalograms we can further examine whether the maxima (minima) occurring in individual events have any systematic behavior or they are occurring at random. We need to study the distributions of the scale parameter, denoted by a_{\max} (a_{\min}), at which such maxima (minima) occurs. Frequency distributions of a_{\max} and a_{\min} are plotted in Figures 5.17 and 5.18, respectively for the ^{16}O -Ag/Br and ^{32}S -Ag/Br interactions with two different bin widths i.e. $\Delta a_{\max/\min} = 0.02$ and $\Delta a_{\max/\min} = 0.04$. In order to better understand the mechanism of cluster formation, experimental results are compared with the UrQMD+BEC simulation. No appreciable difference between the experiment and the corresponding simulation can be seen in these distributions. As such no significant difference in the nature of $a_{\max(\min)}$ distribution is observed between the ^{16}O -Ag/Br and ^{32}S -Ag/Br interactions either, except that the tail of the distributions are stretched a bit more in the ^{16}O -Ag/Br rather than in the ^{32}S -Ag/Br case. Both a_{\max} and a_{\min} distributions are peaked at a very small value like, $a_{\max/\min} \approx 0.1$. The diagrams suggest that the cluster size is always less than one pseudorapidity unit, which perhaps indicates dominance of short range correlations in the data. In the framework of the UrQMD

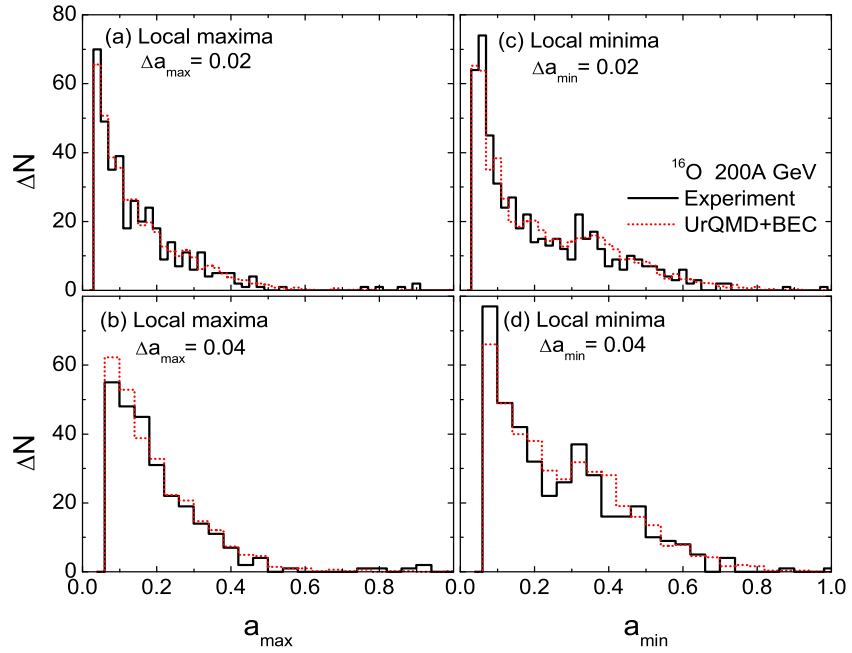


Figure 5.17: Distributions of the local maxima (left) and the local minima (right) of the scalograms in ^{16}O -Ag/Br interactions at 200A GeV/c.

model short range correlations are manifested because of resonance decays, jet fragmentation etc. The pseudorapidity values preferred by the particle clusters are represented by the local maxima seen in the pseudorapidity distributions. This signature is magnified in the

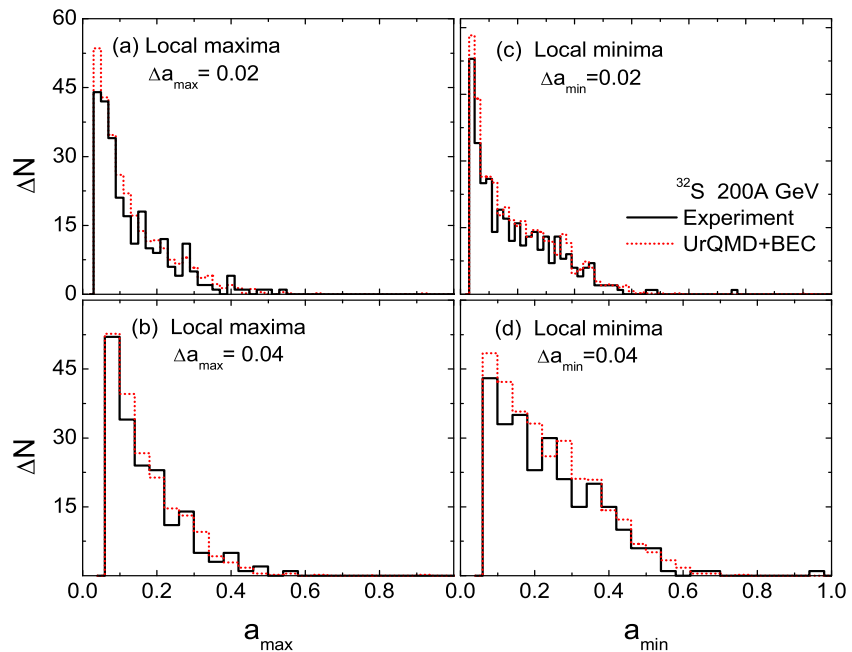


Figure 5.18: The same as in Figure 5.17 but for the ^{32}S -Ag/Br interactions.

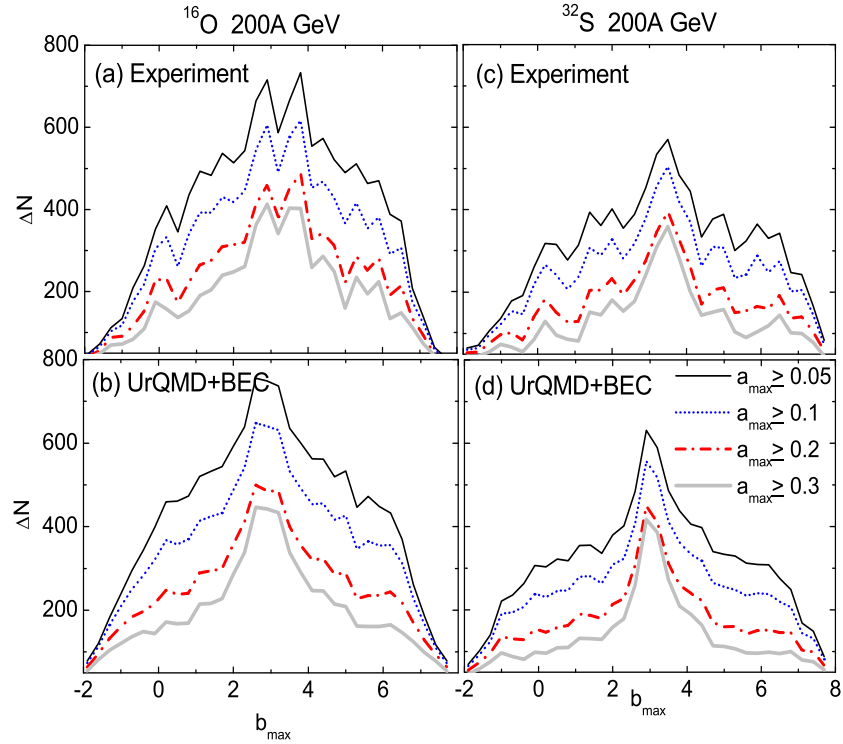


Figure 5.19: Distributions of b_{\max} for different values of a_{\max} cut in ^{16}O -Ag/Br (left) and ^{32}S -Ag/Br (right) interactions at 200A GeV/c. In the lower panel shown are the results from the UrQMD+BEC simulations.

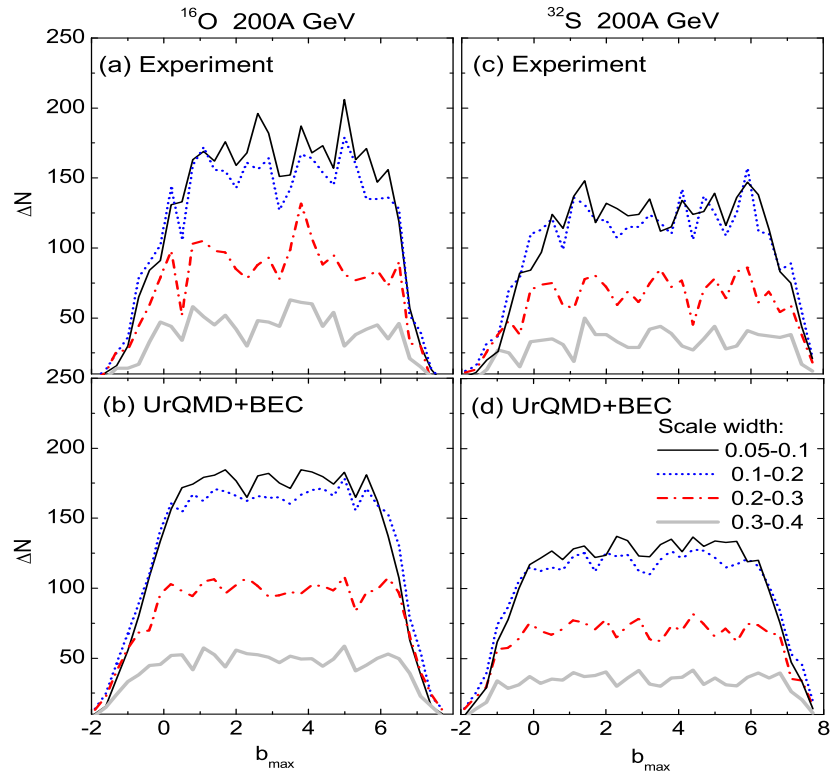


Figure 5.20: The same as in Figure 5.19 but for different scale windows (Δa_{\max}).

distributions of b_{\max} , which actually is the pseudorapidity coordinate of the wavelet maxima $W_{g_2}(a_{\max}, b_{\max})$. We examine the b_{\max} distribution with the help of different choices of a_{\max} cut as well as using different scale intervals. Such distributions for the $^{16}\text{O-Ag/Br}$ and $^{32}\text{S-Ag/Br}$ event samples (both experiment and simulation) are graphically presented in Figure 5.19. It is clear that with increasing a_{\max} the fluctuations get reduced and the patterns become smooth. For all the scale intervals the peaks however remain fixed at the same position. In comparison with the experiment, perhaps due to a larger statistics the UrQMD+BEC distributions vary less rapidly. Otherwise no significant difference between either the experimental and the corresponding simulated distributions, or between the two interactions considered are seen. In Figure 5.20, we plot b_{\max} -distribution for different scale intervals for the experimental and simulated event samples for both interactions. As expected, in all the cases the fluctuations are more in the scale interval $0.05 \leq a \leq 0.1$, which get reduced with increasing a .

5.5 Summary

From the azimuthal structure analysis we find that the average behavior of the S -parameters exhibits unusual structures in both $^{16}\text{O-Ag/Br}$ and $^{32}\text{S-Ag/Br}$ interactions that are limited in narrow regions of η and/or φ -space. Small but significant experimental departure from independent emission model, particularly at small $\delta\eta$ are seen. This suggests that short range correlations are present in the experimental data. In this regard our observation matches with another similar experiment where nuclear emulsion technique was used [11]. A closer look at the distributions of structure size ($\Delta\eta$) and their positions (η_m) indicates that features pertaining to both ring-like and jet-like structures are present in our data samples that cannot be fully reproduced by a simple random number generated independent emission model. The effects however, are always not too strong in either type of interaction concerned. Within the framework of the Cerenkov gluon emission model [1] we can therefore, conclude that in some events there are only a few emitted gluons, whereas in some other their numbers are large. It would be a worthwhile exercise to determine either the nuclear refractive index or the speed of the sound wave in the fireball medium, either of which can further be utilized to find out a proper equation of state of the hadronic/partonic matter.

In the wavelet analysis once again we find significant differences between the experiment and corresponding UrQMD+BEC simulation. For all the parameters studied in connection with the g_2 and g_4 wavelets, usually larger and somewhat ordered fluctuations are observed in both $^{16}\text{O-Ag/Br}$ and $^{32}\text{S-Ag/Br}$ experimental data samples. These differences should be interpreted in terms of certain nontrivial dynamical reason(s), like short range correlation. A detailed and more involved analysis in a higher-dimensional phase space is necessary to

unravel the dynamics of cluster formation more clearly. However, we understand that the wavelet analysis is a powerful statistical tool for an event-by-event analysis of fluctuation patterns in high-energy nuclear collisions.

Bibliography

- [1] I. M. Dremin, *Pis'ma Zh. Eksp. Teor. Fiz.* 30, 152 (1979).
- [2] A. E. Glassgold, W. Heckrotte, K. M. Watson, *Ann. Phys.* 6, 1 (1959).
- [3] I. M. Dremin, *Yad. Fiz.* 33, 1357 (1981).
- [4] I. M. Dremin, *Pis'ma Zh. Eksp. Teor. Fiz.* 34, 594 (1981).
- [5] I. M. Dremin, *Nucl. Phys. A* 467, 233 (2006).
- [6] I. Daubechies, *Ten Lectures on Wavelets: Society for Industrial and Applied Mathematics, Philadelphia* (1992).
- [7] J. C. Van Den Berg (ed.), *Wavelets in Physics: Cambridge University Press* (2004).
- [8] D.-W. Huang, *Phys. Rev. D* 56, 3961 (1997).
- [9] V. V. Uzhinsky *et al.*, *Phys. of Atom. Nucl.* 67, 156 (2004).
- [10] A. B. Apanasenko *et al.*, *Pis'ma Zh. Eksp. Teor. Fiz.* 30, 157 (1979).
- [11] M. I. Adamovich, *et al.* (EMU01 Collaboration), *J. Phys. G* 19, 2035 (1993).
- [12] A. El-Naghy, K. S. Abdel-Khalek, *Phys. Lett. B* 299, 370 (1993).
- [13] G. L. Gogiberidge *et al.*, *Nucl. Phys. B (Proc. Suppl.)* 92, 75 (2001);
- [14] G. L. Gogiberidge, L. K. Gelovani and E. K. Sarkisyan, *Phys. Atom. Nucl.* 64, 143 (2006); *Phys. Lett. B* 430, 368 (1998).
- [15] S. Vokál *et al.*, *Phys. Atom. Nucl.* 71, 1395 (2008).
- [16] S. Vokál, G. I. Orlova and S. Lehocká, *Phys. Atom. Nucl.* 72, 237 (2009).
- [17] G. I. Orlova, *et al.*, *Proc. International Conference Hadron Structure 2002, Herľany, Slovakia, 2002* (P. J. Šafárik Univ., Košice, 2003), p. 155.
- [18] A. Sh. Gaitinov *et al.* (EMU12), *Talk given at XVII. Meeting of the EMU01 Collaboration, Dubna, Russia, May 18-20 (1999).*

-
- [19] S. Vokál, A. Vokálová *et al.*, Proc. Hadron Structure 2004, Smolenice castle, Slovakia, 30.8.-30.9 (2004).
- [20] P. Mali *et al.*, Int. J. Mod. Phys. E 23, 1450027 (2014).
- [21] N. Suzuki, M. Biyajima and A. Ohsawa, Prog. Theor. Phys. 94, 91 (1995).
- [22] Z. Huang *et al.*, Phys. Rev. D 54, 750 (1996).
- [23] B. K. Nandi *et al.* (WA98 Collaboration), in Proc. of the 3rd Intern. Conf. on Physics and Astrophysics of Quark-Gluon Plasma, Jaipur, India, (1997).
- [24] T. H. Burnett *et al.*, Phys. Rev. Lett. 50, 2062 (1983).
- [25] I. M. Dremin, Physics - Uspekhi 43, 1137 (2000).
- [26] O. D. Chernavskaya *et al.* (EMU15 Collaboration), Proc. 24th ICRC, Rome (1996).
- [27] N. M. Astafyeva, I. M. Dremin, K. A. Kotelnikov, Mod. Phys. Lett. A 12, 1185 (1997).
- [28] J. Fedorišin and S. Vokál, JINR Preprint E1-2007-4., Dubna, (2007).
- [29] P. Mali *et al.*, Adv. High Eng. Phys. 2013, 1 (2013).
- [30] J. Fedorišin and S. Vokál, Fizika B 17, 273 (2008).
- [31] E. Stenlund, *et al.* (EMU01 Collaboration), Nucl. Phys. A 498, 541c (1989).